INTERNATIONAL JOURNAL FOR NUMERICAL METHODS IN FLUIDS
Int. J. Numer. Meth. Fluids 2010; **63**:1–21
Published online 27 May 2009 in Wiley InterScience (www.interscience.wiley.com). DOI: 10.1002/fld.2069

Implementation of semi-discrete, non-staggered central schemes in a colocated, polyhedral, finite volume framework, for high-speed viscous flows

Christopher J. Greenshields[1, 2, *, †], Henry G. Weller[2], Luca Gasparini[3] and Jason M. Reese[1]

[1]*Department of Mechanical Engineering, University of Strathclyde, Glasgow G1 1XJ, U.K.*
[2]*OpenCFD Ltd., 9 Albert Road, Caversham, Reading RG4 7AN, U.K.*
[3]*Fondmetal Technologies S.r.l., Via Bondenese 31, 44041 Casumaro (FE), Italy*

SUMMARY

We describe the implementation of a computational fluid dynamics solver for the simulation of high-speed flows. It comprises a finite volume (FV) discretization using semi-discrete, non-staggered central schemes for colocated variables prescribed on a mesh of polyhedral cells that have an arbitrary number of faces. We describe the solver in detail, explaining the choice of variables whose face interpolation is limited, the choice of limiter, and a method for limiting the interpolation of a vector field that is independent of the coordinate system. The solution of momentum and energy transport in the Navier–Stokes equations uses an operator-splitting approach: first, we solve an explicit predictor equation for the convection of conserved variables, then an implicit corrector equation for the diffusion of primitive variables. Our solver is validated against four sets of data: (1) an analytical solution of the one-dimensional shock tube case; (2) a numerical solution of two dimensional, transient, supersonic flow over a forward-facing step; (3) interferogram density measurements of a supersonic jet from a circular nozzle; and (4) pressure and heat transfer measurements in hypersonic flow over a 25°–55° biconic. Our results indicate that the central-upwind scheme of Kurganov, Noelle and Petrova (*SIAM J. Sci. Comput.* 2001; **23**:707–740) is competitive with the best methods previously published (e.g. piecewise parabolic method, Roe solver with van Leer limiting) and that it is inherently simple and well suited to a colocated, polyhedral FV framework. Copyright © 2009 John Wiley & Sons, Ltd.

Received 11 November 2008; Revised 10 March 2009; Accepted 24 March 2009

KEY WORDS: finite volume; polyhedral; semi-discrete; central schemes; hypersonic flows; biconic; supersonic jet; forward-facing step; compressible viscous flows; Navier–Stokes equations

*Correspondence to: Christopher J. Greenshields, Department of Mechanical Engineering, University of Strathclyde, Glasgow G1 1XJ, U.K.
†E-mail: c.greenshields@opencfd.co.uk, chris.greenshields@strath.ac.uk

Contract/grant sponsor: UK's Engineering and Physical Sciences Research Council; contract/grant number: EP/F014155/01

1. INTRODUCTION

The development of computational fluid dynamics (CFD) methods for industrial use is mainly driven by demands to perform simulations on large, complex, 3D geometries and to model complex physical behaviour and flow systems. The finite volume (FV) method is generally preferred for industrial CFD because it is relatively inexpensive and lends itself well to solution of large sets of equations associated with complex flows, and to parallel solution by domain decomposition. Usually, solution variables such as velocity and pressure are *colocated*, i.e. they are specified at the same set of discrete locations (the cell centres), e.g. [1, 2]. Colocation is popular in industrial CFD, because it allows greater freedom in mesh structure for complex 3D geometries and for features such as refinement, grading and surface layers. Today there is a preference for unstructured meshes of polyhedral cells with six faces (hexahedra) or more, rather than tetrahedral cells that are prone to numerical inaccuracy and other problems, and are unsuitable for features such as boundary layers [3]. It is no coincidence that colocated, polyhedral, FV numerics are adopted by several of the best known industrial CFD software packages, including FLUENT®, STAR CCM+® and OPENFOAM®.

The presence of discontinuities, such as shocks and contact surfaces, in high-speed compressible flows requires numerical schemes that can capture these features while avoiding spurious oscillations. Notable methods that are effective in producing accurate non-oscillatory solutions are: monotone upstream-centred schemes for conservation laws [4]; piecewise parabolic method (PPM) [5]; essentially non-oscillatory (ENO) schemes [6]; weighted ENO (WENO) schemes [7]; and the Runge–Kutta discontinuous Galerkin (RKDG) method [8]. The methods typically involve Riemann solvers, characteristic decomposition and Jacobian evaluation, making them complex and difficult to implement in a colocated, polyhedral framework.

However, an alternative approach for accurate, non-oscillatory solution exists, using the so-called *central* schemes, which does not involve Riemann solvers or characteristic decomposition, and can avoid Jacobian evaluation. These central schemes were proposed by Nessyahu and Tadmor [9] as a second-order generalization of the Lax–Friedrichs scheme. The method has been developed for multi-dimensional systems and unstructured meshes, principally using vertex-staggered (or overlapping) meshes of triangles [10–16], tetrahedra [17, 18], quadrilaterals [13, 16, 19–24] and hexahedra [25]. However, the staggered approach requires generation of a dual mesh: it can be difficult to ensure quality of both these meshes, particularly at boundaries of 3D geometries that contain complex features such as sharp edges or corners. For these reasons, this paper investigates whether it is possible to simulate compressible flows and performs shock capturing reliably in a *colocated*, polyhedral, FV framework using central schemes. We require that the method can be used for steady-state or diffusion-dominated problems, thus are concerned only with semi-discrete, non-staggered central scheme formulations, beginning with that of Kurganov and Tadmor (KT) [26]. The present paper begins by describing a generic implementation of semi-discrete central schemes on polyhedral meshes and then goes on to test the method on a range of compressible flow cases.

2. GOVERNING EQUATIONS

We wish to solve the standard governing fluid equations in an Eulerian frame of reference:

- *Conservation of mass*:

$$\frac{\partial \rho}{\partial t} + \nabla \cdot [\mathbf{u}\rho] = 0 \tag{1}$$

DOI: 10.1002/fld

- *Conservation of momentum* (*neglecting body forces*):

$$\frac{\partial(\rho\mathbf{u})}{\partial t}+\nabla\cdot[\mathbf{u}(\rho\mathbf{u})]+\nabla p+\nabla\cdot\mathbf{T}=\mathbf{0} \tag{2}$$

- *Conservation of total energy*:

$$\frac{\partial(\rho E)}{\partial t}+\nabla\cdot[\mathbf{u}(\rho E)]+\nabla\cdot[\mathbf{u}p]+\nabla\cdot(\mathbf{T}\cdot\mathbf{u})+\nabla\cdot\mathbf{j}=0 \tag{3}$$

where ρ is the mass density, $\mathbf{u}$ is the fluid velocity, p is the pressure; the total energy density $E=e+|\mathbf{u}|^2/2$ with e the specific internal energy, $\mathbf{j}$ is the diffusive flux of heat, $\mathbf{T}$ is the viscous stress tensor, defined as positive in compression.

In the case of inviscid flows, $\mathbf{T}=\mathbf{0}$ and $\mathbf{j}=\mathbf{0}$, and Equations (1)–(3) reduce to Euler's equations. For viscous flows, the stress tensor can be represented by Newton's law (assuming zero bulk viscosity)

$$\mathbf{T}=-2\mu\,\mathrm{dev}(\mathbf{D}) \tag{4}$$

where μ is the dynamic viscosity, the deformation gradient tensor $\mathbf{D}\equiv\frac{1}{2}[\nabla\mathbf{u}+(\nabla\mathbf{u})^{\mathrm{T}}]$ and its deviatoric component $\mathrm{dev}(\mathbf{D})\equiv\mathbf{D}-(\frac{1}{3})\,\mathrm{tr}(\mathbf{D})\mathbf{I}$, where $\mathbf{I}$ is the unit tensor. The diffusive flux of heat can be represented by Fourier's law

$$\mathbf{j}=-k\nabla T \tag{5}$$

where T is the temperature and k is the conductivity. The Navier–Stokes equations are produced by the substitution of the viscous and heat conduction constitutive relations, Equations (4) and (5), respectively, into the governing equations.

In this paper we consider only a calorically perfect gas for which $p=\rho RT$ and $e=c_vT=(\gamma-1)RT$, where R is the gas constant and $\gamma=c_p/c_v$ is the ratio of specific heats at constant pressure and volume, c_p and c_v, respectively.

3. COMPUTATIONAL METHOD

We use the FV method ascribed on meshes of polyhedral cells with an arbitrary number of faces, each with an arbitrary number of vertices. The spatial domain is therefore divided into a number of contiguous control volumes or cells. In general, there is no alignment of the mesh with the co-ordinate system and the number of neighbouring cells can vary from cell to cell. The only general statement that can be made about cell connectivity is that a cell face is either *internal* and intersects two cells only, or comprises part of an external *boundary* and belongs to a single cell only. In presenting the numerical scheme, we must dispense with notations based on nodal values at 'j' and 'k' or those based on points of the compass, etc., and instead present generic expressions based on cell and face interpolated values.

We assign each face as an owner cell and a neighbour cell. The face area vector $\mathbf{S}_f$ is a vector normal to the face surface pointing out of the owner cell, whose magnitude is that of the area of the face, as shown in Figure 1. In this colocated system, all dependent variables and material properties are stored at each cell centroid, e.g. 'P' in Figure 1. The vector $\mathbf{d}$ connects the centroid

DOI: 10.1002/fld

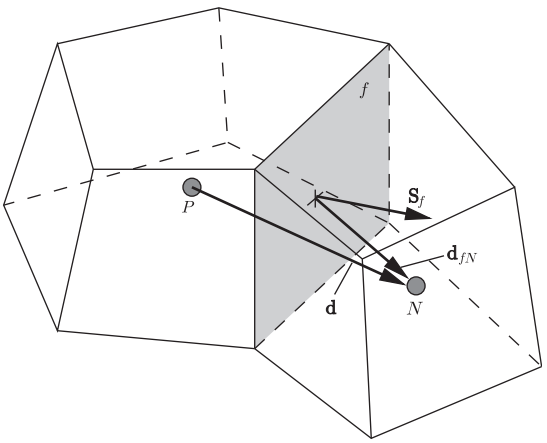

Figure 1. Finite volume discretization.

of the owner cell P to that of neighbouring cell N and the vector $\mathbf{d}_{fN}$ connects the centre of the face to the centroid of the cell N.

Application of the FV method begins by expressing the differential equations we wish to solve within an integral over a cell volume V, assumed fixed in space in this paper. Divergence and gradient terms are then converted to integrals over the cell surface S using a generalized form of Gauss's theorem. The integration requires fluxes at cell faces, evaluated by interpolation of cell centre values to the faces. For polyhedra with an arbitrary number of faces, it is desirable that the interpolation to a given face is between owner and neighbour cells only, otherwise it becomes excessively complex. The second-order semi-discrete, non-staggered schemes of KT [26] and Kurganov, Noelle and Petrova (KNP) [27] permit this. They can ultimately be described as *interpolation* procedures rather than processes of 'reconstruction', 'evolution' and 'projection'. There is therefore no need for a mathematical notation for polynomial functions, hence in the following sections we simply describe the discretization of a general dependent tensor field $\boldsymbol{\Psi}$ of any rank by interpolation of values $\boldsymbol{\Psi}_P$ at cell centres to values $\boldsymbol{\Psi}_f$ at cell faces.

In the present study we are principally concerned with the spatial accuracy of the schemes under investigation. Therefore, time derivatives are discretized by a simple Euler implicit scheme rather than more elaborate methods, such as higher-order Runge–Kutta time integration; there is, however, no difficulty in incorporating such methods for time integration.

3.1. Convective terms

The convective terms in Equations (1)–(3) are $\nabla\cdot[\mathbf{u}\rho]$, $\nabla\cdot[\mathbf{u}(\rho\mathbf{u})]$, $\nabla\cdot[\mathbf{u}(\rho E)]$ and $\nabla\cdot[\mathbf{u}p]$. Their treatment is a critical aspect of central schemes. Each is integrated over a control volume and linearized as follows:

$$\int_V \nabla\cdot[\mathbf{u}\boldsymbol{\Psi}]\,\mathrm{d}V = \int_S \mathrm{d}\mathbf{S}\cdot[\mathbf{u}\boldsymbol{\Psi}] \approx \sum_f \mathbf{S}_f\cdot\mathbf{u}_f\boldsymbol{\Psi}_f = \sum_f \phi_f\boldsymbol{\Psi}_f \tag{6}$$

where $\sum_f$ denotes a summation over cell faces and $\phi_f = \mathbf{S}_f\cdot\mathbf{u}_f$ is the volumetric flux, i.e. the volume of fluid flowing through the face per second. The simplest method for evaluating $\mathbf{u}_f$ and

DOI: 10.1002/fld

$\boldsymbol{\Psi}_f$, often used for incompressible flows, is: linear interpolation of $\mathbf{u}$ from neighbouring cells (central differencing); interpolation of $\boldsymbol{\Psi}$ according to one of many schemes that usually use some degree of upwinding to stabilize the solution. The upwind direction is based on the flow velocity and hence is characterized by the sign of ϕ_f. Linear interpolation of $\boldsymbol{\Psi}$ is evaluated using the weighting coefficient $w_f = |\mathbf{S}_f \cdot \mathbf{d}_{fN}|/|\mathbf{S}_f \cdot \mathbf{d}|$, according to

$$\boldsymbol{\Psi}_f = w_f \boldsymbol{\Psi}_P + (1 - w_f)\boldsymbol{\Psi}_N$$

For compressible flows, however, fluid properties are not only transported by the flow, but also by the propagation of waves. This requires the flux interpolation to be stabilized based on transport that can occur in any direction. Since we are interpolating to a given face only from neighbouring cell values, we apply the KT and KNP methods in their original form for multi-dimensional systems using the so-called 'dimension-by-dimension' reconstruction [26, 27] (perhaps better termed as 'face-by-face' reconstruction in a polyhedral framework), rather than some genuinely multi-dimensional form of reconstruction [15].

The interpolation procedure is split into two directions corresponding to flow outward and inward of the face owner cell. We denote these directions $f+$, coinciding with the direction $+\mathbf{S}_f$, and $f-$, coinciding with $-\mathbf{S}_f$. The discretization is as follows:

$$\sum_f \phi_f \boldsymbol{\Psi}_f = \sum_f [\alpha \phi_{f+} \boldsymbol{\Psi}_{f+} + (1-\alpha)\phi_{f-} \boldsymbol{\Psi}_{f-} + \omega_f (\boldsymbol{\Psi}_{f-} - \boldsymbol{\Psi}_{f+})] \tag{7}$$

The first two terms on the right-hand side of Equation (7) are flux evaluations in the $f+$ and $f-$ directions, respectively. The third term is strictly only required in cases where the convection term is a part of a substantive derivative, e.g. $\nabla \cdot [\mathbf{u}(\rho \mathbf{u})]$ in Equation (2), for which $\partial(\rho \mathbf{u})/\partial t$ completes the substantive derivative of $\rho \mathbf{u}$. It is an additional diffusion term using a volumetric flux ω_f based on the maximum speed of propagation of any discontinuity that may exist at a face between values interpolated in the $f+$ and $f-$ directions.

In the KT method, the $f+$ and $f-$ contributions are weighted equally so that the weighting coefficient is $\alpha = 0.5$, hence its description as a *central* scheme. The KNP method calculates α based on one-sided local speeds of propagation. The weighting is then biased in the upwind direction, hence these schemes are termed as *central upwind*. Volumetric fluxes associated with the local speeds of propagation can be calculated as follows, noting that they are both defined here as positive in their respective directions $f+$ and $f-$:

$$\begin{aligned} \psi_{f+} &= \max(c_{f+}|\mathbf{S}_f| + \phi_{f+},\ c_{f-}|\mathbf{S}_f| + \phi_{f-},\ 0) \\ \psi_{f-} &= \max(c_{f+}|\mathbf{S}_f| - \phi_{f+},\ c_{f-}|\mathbf{S}_f| - \phi_{f-},\ 0) \end{aligned} \tag{8}$$

Here, $c_{f\pm} = \sqrt{\gamma R T_{f\pm}}$ are the speeds of sound of the gas at the face, outward and inward of the owner cell. The weighting factor is:

$$\alpha = \begin{cases} \dfrac{1}{2} & \text{for the KT method} \\ \dfrac{\psi_{f+}}{\psi_{f+} + \psi_{f-}} & \text{for the KNP method} \end{cases} \tag{9}$$

DOI: 10.1002/fld

The diffusive volumetric flux is calculated according to:

$$\omega_f = \begin{cases} \alpha \max(\psi_{f+}, \psi_{f-}) & \text{for the KT method} \\ \alpha(1-\alpha)(\psi_{f+} + \psi_{f-}) & \text{for the KNP method} \end{cases} \tag{10}$$

The method involves $f+$ and $f-$ face interpolations of a number of variables (T, ρ, etc.) from values at neighbouring cell centres. The interpolation procedure uses a limiter to switch between low- and high-order schemes based on a flux limiter function $\beta(r)$, where r represents the ratio of successive gradients of the interpolated variable, constrained to $r \geqslant 0$. On a polyhedral mesh, r can be described as follows for the $f+$ direction:

$$r = 2\frac{\mathbf{d} \cdot (\nabla \boldsymbol{\Psi})_P}{(\nabla_{\mathbf{d}} \boldsymbol{\Psi})_f} - 1 \quad \text{(scalar } \boldsymbol{\Psi}\text{)} \tag{11}$$

where $(\nabla \boldsymbol{\Psi})_P$ is the full gradient calculated at the owner cell P as described in Section 3.2 with linear interpolation and $(\nabla_{\mathbf{d}} \boldsymbol{\Psi})_f = \boldsymbol{\Psi}_N - \boldsymbol{\Psi}_P$ is the gradient component normal to the face, scaled by $|\mathbf{d}|$.

The $f+$ and $f-$ interpolations in this paper are based on limiting standard first-order upwind and second-order linear interpolations. We choose limiters that are total variation diminishing (TVD) and symmetric, for which $\beta(r)/r = \beta(1/r)$, namely Minmod [28] and van Leer [29], whose limiter functions are $\beta(r) = \max[0, \min(1, r)]$ and $\beta(r) = (r + |r|)/(1 + r)$, respectively. Then, the $f+$ interpolation of $\boldsymbol{\Psi}$, for example, is simply evaluated as

$$\boldsymbol{\Psi}_{f+} = (1 - g_{f+})\boldsymbol{\Psi}_P + g_{f+}\boldsymbol{\Psi}_N$$

where $g_{f+} = \beta(1 - w_f)$. It is evident that $\beta = 0$ gives upwind interpolation and $\beta = 1$ gives linear interpolation; it should also be noted that $0 \leqslant \beta \leqslant 2$, such that $\beta = 2$ corresponds to downwind interpolation.

3.2. Gradient terms

The gradient terms present in the fluid governing equations include ∇p in Equation (2). Such terms are usually integrated over a control volume and discretized as follows:

$$\int_V \nabla \boldsymbol{\Psi} \, \mathrm{d}V = \int_S \mathrm{d}\mathbf{S}\boldsymbol{\Psi} \approx \sum_f \mathbf{S}_f \boldsymbol{\Psi}_f \tag{12}$$

For incompressible flows, $\boldsymbol{\Psi}_f$ is typically calculated by linear interpolation. The KT and KNP schemes, however, split the interpolation procedure into $f+$ and $f-$ directions according to:

$$\sum_f \mathbf{S}_f \boldsymbol{\Psi}_f = \sum_f [\alpha \mathbf{S}_f \boldsymbol{\Psi}_{f+} + (1 - \alpha)\mathbf{S}_f \boldsymbol{\Psi}_{f-}] \tag{13}$$

The $f+$ and $f-$ interpolation uses the limiter described in the previous section.

DOI: 10.1002/fld

3.3. Laplacian terms

For the sake of completeness, it is worth describing the discretization of Laplacian terms with diffusion coefficient Γ for polyhedral meshes. They are initially discretized as follows:

$$\int_V \nabla\cdot(\Gamma\nabla\boldsymbol{\Psi})\,\mathrm{d}V = \int_S \mathrm{d}\mathbf{S}\cdot(\Gamma\nabla\boldsymbol{\Psi}) \approx \sum_f \Gamma_f \mathbf{S}_f\cdot(\nabla\boldsymbol{\Psi})_f \tag{14}$$

Usually, Γ_f is interpolated linearly from the cell centre values. For the general case that a face is non-orthogonal (i.e. $\mathbf{S}_f$ is not parallel to $\mathbf{d}$), the evaluation of $\mathbf{S}_f\cdot(\nabla\boldsymbol{\Psi})_f$ is split into an orthogonal component in terms of neighbour and owner cell values, and a non-orthogonal component in terms of a full gradient, calculated at cell centres and itself interpolated to the face, i.e.

$$\mathbf{S}_f\cdot(\nabla\boldsymbol{\Psi})_f = \underbrace{A(\boldsymbol{\Psi}_N-\boldsymbol{\Psi}_P)}_{\text{orthogonal}} + \underbrace{\mathbf{a}\cdot(\nabla\boldsymbol{\Psi})_f}_{\text{non-orthogonal}} \tag{15}$$

where $A=|\mathbf{S}_f|^2/(\mathbf{S}_f\cdot\mathbf{d})$ and $\mathbf{a}=\mathbf{S}_f-A\mathbf{d}$.

3.4. Boundary conditions

Boundary conditions are applied as follows. For a Dirichlet condition a fixed value $\boldsymbol{\Psi}_b$ is specified at the boundary. The discretization of a convection term requires the value of $\boldsymbol{\Psi}$ at all faces, in which case $\boldsymbol{\Psi}_b$ may be directly substituted at such a boundary face. The discretization of a Laplacian term requires the normal gradient of $\boldsymbol{\Psi}$ at each face, which is evaluated at a boundary face by differencing $\boldsymbol{\Psi}_b$ and $\boldsymbol{\Psi}_i$, where i denotes the cell adjacent to the boundary face.

For a Neumann condition, a fixed normal gradient $(\mathbf{n}\cdot\nabla\boldsymbol{\Psi})_b$ is specified at the boundary. This can be directly substituted at such a boundary face for the discretization of an Laplacian term. For a convection term, a boundary face value must be evaluated by extrapolation from $\boldsymbol{\Psi}_i$ using the normal gradient.

3.5. Implementation in OpenFOAM

Based on the computational method described above, we wrote a solver called `rhoCentralFoam`, released with version 1.5 of OpenFOAM [30], the open source CFD toolbox. Written in C++, OpenFOAM uses FV numerics to solve systems of partial differential equations ascribed on any three-dimensional unstructured mesh of polygonal cells. All solvers developed within OpenFOAM are, by default, three dimensional, but can be used for one- or two-dimensional problems by the application of particular conditions on boundaries lying in the plane of the direction(s) of no interest. In this paper we choose specific validation cases that present particular practical difficulties that need to be met by a robust solver for real, engineering applications.

4. INVISCID SOLVER

Initially, we developed a solver for inviscid flow and tested it on the shock tube problem of Sod [31] to make a general assessment of its accuracy. It is worth stating that this problem is of limited use because it is one dimensional and, with a Mach number approaching 0.9 in critical regions, it does not provide a strong test of the solver's ability to control oscillations due to disturbances

DOI: 10.1002/fld

travelling in the direction opposing the flow. Indeed, good solutions may be obtained for the shock tube problem without any form of flux splitting.

Instead, some regions of low-speed flow are needed to test the handling of the propagation of disturbances in the direction opposing the flow. Two-dimensional supersonic problems generally provide a better test of shock-capturing capability and, while there is no propagation of disturbances upstream of the principal flow direction, disturbances can freely travel in the transverse direction, transporting spurious oscillations in the process. We therefore chose the forward step problem of Woodward and Colella [32] to investigate the oscillatory behaviour of the solver and, additionally, difficulties associated with flow around sharp corners.

For the inviscid solver, the set of governing equations in Section 2 is solved explicitly in an iterative sequence. We solve for density-weighted fields: ρ, momentum density $\hat{\mathbf{u}}=\rho\mathbf{u}$, and total energy density $\hat{E}=\rho E$.

An important issue when solving the set of equations for ρ, $\hat{\mathbf{u}}$ and $\hat{E}$ in an iterative sequence is maintaining boundedness on T. A problem arises because T is evaluated by the subtraction of kinetic energy from the total energy according to:

$$T=\frac{1}{c_v}\left(\frac{\hat{E}}{\rho}-\frac{|\mathbf{u}|^2}{2}\right) \tag{16}$$

With the decoupling of solutions for $\hat{\mathbf{u}}$ and $\hat{E}$, which includes some values lagged from old times, there is the possibility that T can fall below 0 and the solution fail. During the early stages of our solver development, it became apparent that a good strategy to prevent unboundedness in T was to construct $f+$ and $f-$ interpolations of $\hat{E}$ from $f+$ and $f-$ interpolations of ρ, $\hat{\mathbf{u}}$ and T in the discretization of $\nabla\cdot(\mathbf{u}\hat{E})$. In the $f+$ direction, for example, rather than directly interpolate $\hat{E}$ itself, we evaluate $\hat{E}_{f+}=\rho_{f+}(c_vT_{f+}+|(\hat{\mathbf{u}}_{f+}/\rho_{f+})^2|/2)$. In all, only ρ, $\hat{\mathbf{u}}$ and T were interpolated to faces in the $f+$ and $f-$ directions. Fluxes of other fields interpolated in the $f+$ and $f-$ directions were calculated from those for ρ, $\hat{\mathbf{u}}$ and T, e.g. $p_{f+}=\rho_{f+}RT_{f+}$.

4.1. The shock tube problem

The first validation case is that of unsteady wave motion in a shock tube. In this problem, a diaphragm separates a region of high-pressure gas to the left, denoted by subscript L, from a region of low-pressure gas to the right, denoted by subscript R. When the diaphragm is broken, a shock wave propagates into the low-pressure region from left to right and an expansion wave propagates into the high-pressure region from right to left. An analytical solution is available for this transient problem if the shock tube is idealized as one dimensional and the gas considered calorically perfect [33]. Sod [31] adopted a case setup in which the gas was initially at rest with $\rho_L=1.0$ and $\rho_R=0.125$. We followed this setup with $p_L=10^5\,\mathrm{Pa}$ and $p_R=10^4\,\mathrm{Pa}$, so that for $R=287\,\mathrm{J/(kg\,K)}$, $T_L=348.4\,\mathrm{K}$ and $T_R=278.7\,\mathrm{K}$. Our solution domain was one dimensional in the range $-5\,\mathrm{m}\leqslant x\leqslant 5\,\mathrm{m}$, with the diaphragm located at $x=0\,\mathrm{m}$. A coarse mesh of 100 cells was used in order to highlight the relative accuracy of different numerical schemes. The case was run with a fixed time step corresponding to a Courant–Friedrichs–Lewy (CFL) number 0.2, below the stability limit of 0.5 of the central schemes. Results are presented here for ρ at time $t=7\,\mathrm{ms}$.

The first set of test simulations compared the purely central KT scheme with the central-upwind KNP scheme. The face interpolations for the $f+$ and $f-$ flux evaluations were calculated using the Minmod limiter, which are the scheme generally cited in the principal references to the KT

DOI: 10.1002/fld

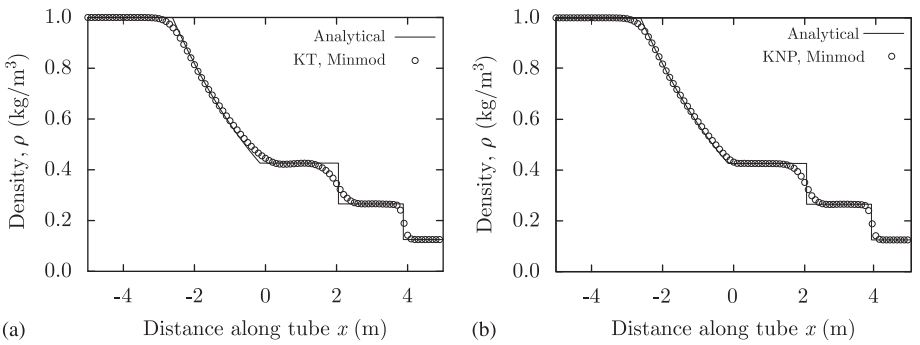

Figure 2. Comparison of shock tube density profile results for KT and KNP schemes with Minmod limiter; CFL number 0.2: (a) KT scheme and (b) KNP scheme.

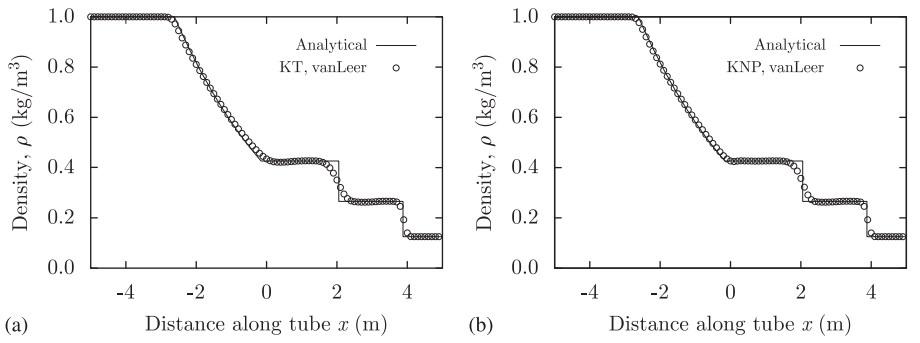

Figure 3. Comparison of shock tube density profile results for KT and KNP schemes with van Leer limiter; CFL number 0.2: (a) KT scheme and (b) KNP scheme.

[26] and KNP [27] methods. Our results in Figure 2 show smooth solutions for both methods, with very good resolution of the shock. The results for the KNP method are, however, clearly more accurate. In particular, the upstream and downstream ends of the expansion are resolved much better with the KNP method, and the contact region is less diffuse.

On switching from the Minmod to the van Leer limiter, the results in Figure 3 show better resolution while not sharpening solutions excessively in diffuse regions, as expected. As before, the KNP method yields more accurate results than the KT method, particularly in the resolution of the expansion corners and contact region. The accuracy is significantly better using the van Leer limiter than using Minmod, even to the extent that the KT method with van Leer limiter produces more accurate solutions than the KNP method with Minmod.

For such a simple, non-Riemann-type method, the KNP approach with van Leer limiter produces impressive solutions that are non-oscillatory and generally accurate. It is only at the contact region (at $x \approx 2$ in Figures 2 and 3), which the accuracy of the scheme is questionable. The shock tube problem therefore informs our initial choice of a solver using the KNP method with a van Leer flux limiter. In the next section we examine and develop our solver further through tests on a two-dimensional problem.

DOI: 10.1002/fld

4.2. The forward step problem (Woodward and Colella)

The case of uniform Mach 3 flow in a wind tunnel containing a forward-facing step was originally introduced by Emery [34] as a test for numerical schemes and later adopted by Woodward and Colella [32]. The wind tunnel is 1 unit length high and 3 units long. The step is 0.2 units high and is located 0.6 units from the inlet on the left. The tunnel is assumed to be infinitely wide in the direction orthogonal to the computational plane. The case uses a gas with $\gamma = 1.4$ and is initialized with $p = 1$, $T = 1$ and Mach 3. For simplicity, we set $R = \gamma^{-1} = 0.714$, so that the speed of sound $c = \sqrt{\gamma RT} = 1$, and the flow velocity $\mathbf{u} = (3, 0, 0)$ corresponds directly to the Mach number.

Woodward and Colella presented their results using the PPM with Lagrangian Remap (PPMLR) [5], a form of non-linear Riemann solver that is generally considered very accurate. Their method includes an applied 'fix' to eliminate unphysical production of entropy at the step corner that results in an 'entropy layer' along the step surface and a spurious Mach stem. The KNP method we use here includes no entropy fix. Cockburn and Shu [8] similarly applied no such fix when applying their RKDG solver to the forward step case. Their results using the third-order P^2 scheme on a mesh of rectangular cells exhibited high accuracy, particularly at contact surfaces.

Woodward and Colella discretized the tunnel height into a regular mesh of 80 cells, with 240 along the length, to produce a mesh of square cells of side length $\frac{1}{80}$. Cockburn and Shu refined the mesh further to a cell length of $\frac{1}{160}$. We therefore ran simulations on both these mesh densities to enable direct comparison between PPMLR with entropy fix, RKDG, and the numerical method presented here. We ran the simulations at a CFL number of 0.2.

4.2.1. TVD schemes for vector fields. Where face interpolation of a non-scalar field, such as $\mathbf{u}$, is required, there is some flexibility in how the limiting is performed. A common approach is to limit each component of the field separately, calculating a different r, and hence $\beta(r)$, for each component. This approach is questionable since it must produce solutions that vary depending on the orientation of the coordinate system. We therefore sought an alternative approach that uses

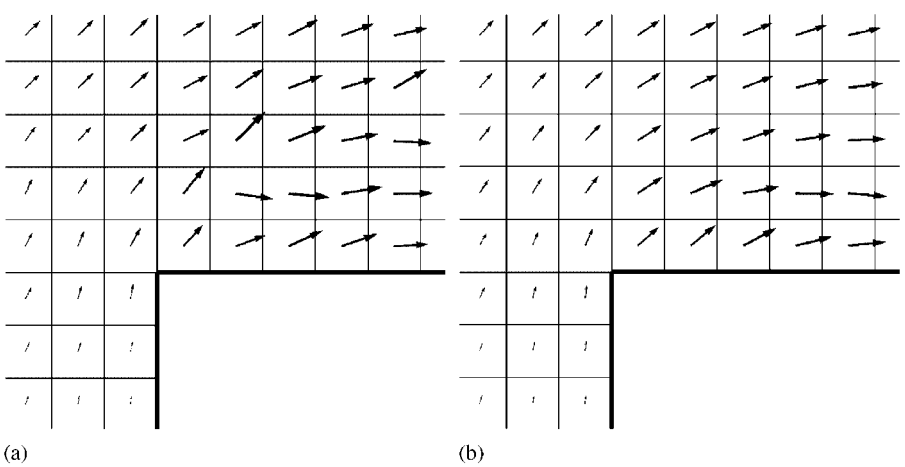

Figure 4. Velocity near step corner with and without 'V'-scheme, van Leer limiter, $t = 0.15$ s (glyphs scaled by $0.003|\mathbf{u}|$): (a) Non-'V'-scheme and (b) 'V'-scheme.

DOI: 10.1002/fld

the same limiter on all components to make it invariant under a coordinate transformation. Initial attempts involved choosing a function to convert the vector field, e.g. $\mathbf{u}$, to a scalar field from which a single r could be calculated by Equation (11). This approach was generally unsuccessful: for example, calculating $r(\boldsymbol{\Psi})$ based on $\boldsymbol{\Psi}=|\mathbf{u}|$ was found to be unstable in the forward step case, with T falling below the lower bound of 0 K at $t=0.165$ s in cells along the top surface of the step adjacent to the corner. Figure 4(a) shows a vector plot of velocity in cells in that region at $t=0.15$ s, in which there is a clear evidence of oscillations in the velocity as the flow moves past the step corner. This result suggests insufficient limiting in a region of high-flow curvature.

We therefore propose here an alternative method to maximize the limiting based on the 'worst-case' direction, i.e. the direction of steepest gradient in $\boldsymbol{\Psi}$ at the cell face. This results in a single expression for r for a vector field:

$$r=2\frac{(\nabla\boldsymbol{\Psi})_f\cdot\mathbf{d}\cdot(\nabla\boldsymbol{\Psi})_P}{(\nabla_{\mathbf{d}}\boldsymbol{\Psi})_f\cdot(\nabla_{\mathbf{d}}\boldsymbol{\Psi})_f}-1 \quad \text{(vector } \boldsymbol{\Psi}\text{)} \tag{17}$$

This generic scheme for TVD limiting of vector fields, which we term the *V-scheme*, produces stable solutions in the forward step case. Figure 4(b) shows a comparative vector plot of velocity in cells adjacent to the step corner in which the oscillations have clearly disappeared. We therefore adopted the V-scheme to limit the interpolation of vector fields in all subsequent simulations presented in this paper.

4.2.2. Results. The solution to this problem evolves from $t=0$ to $t=4$ as shown in Figure 5: (a) a detached bow shock immediately develops ahead of the step, initially curving strongly towards the upper surface of the step; (b) the curvature of the bow shock decreases rapidly and strikes the upper boundary of the domain; (c) the shock is reflected downwards and strikes the upper surface of the step; (d) the bow shock continues to flatten until its incident angle to the upper boundary of the domain is so large that a Mach reflection forms; and (e–h) the point of intersection of incident, normal and reflected waves gradually moves upstream and away from the upper surface—a slip surface separating regions of different velocity emanates horizontally from the intersecting shocks. There also exists a weak shock formed where the overexpanded flow around the step corner strikes the upper surface of the step.

Woodward and Colella and Cockburn and Shu, presented results for density at $t=4$. Figure 6 compares their results with those from our KNP method with van Leer limiting. All methods capture the principal features of the flow, agreeing on the locations of those features and resolving the shocks to a similar thickness (considering the different mesh densities in the figures). The area in which the KNP method is apparently inferior to PPMLR and RKDG is in the resolution of the slip discontinuity: even with an additional level of refinement in Figure 6(c) compared with Figure 6(a) the discontinuity is more diffuse than with PPMLR, and the RKDG method clearly resolves the slip discontinuity extremely well.

The entropy fix in the PPMLR eliminates the Mach stem at the upper surface of the step, whereas a Mach stem is clearly visible in the solutions of our KNP method and the RKDG method. As one would expect, the stem length decreases as the entropy layer decreases with mesh refinement. The Mach stem is longer in the RKDG method than in our KNP method.

DOI: 10.1002/fld

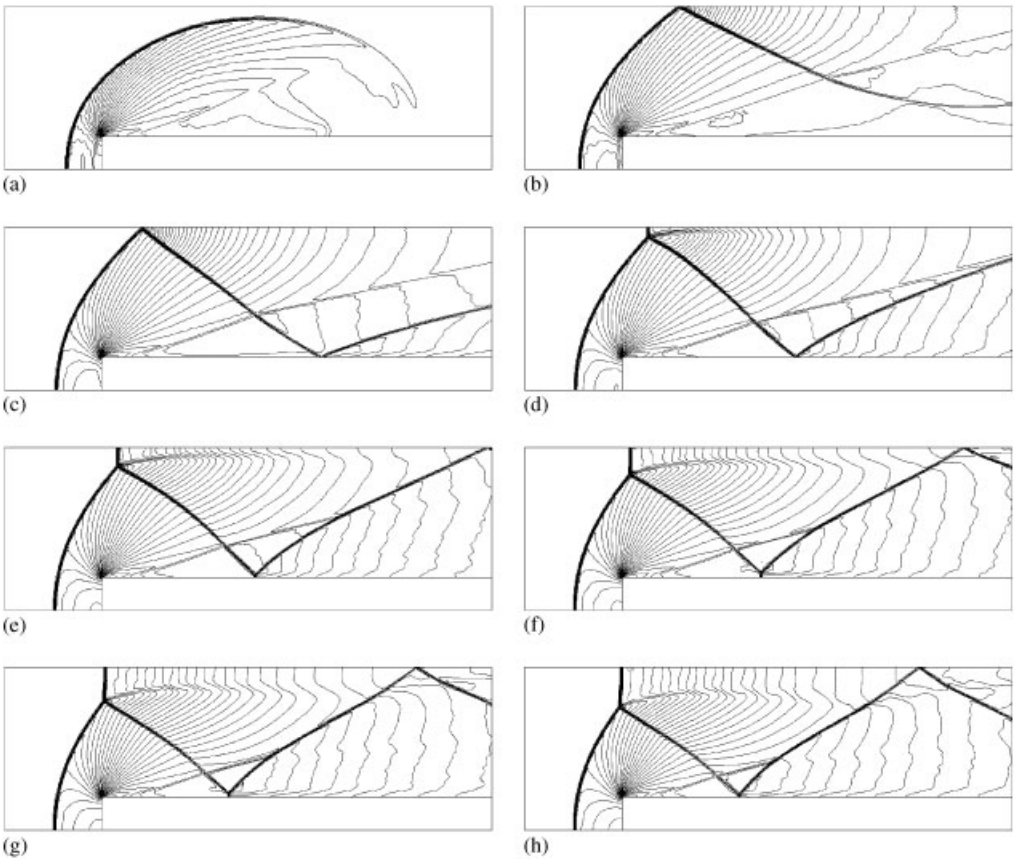

Figure 5. Forward-facing step, transient flow solutions at various times, t; cell size$=\frac{1}{160}$; 40 density contours in the range $0<\rho<8$: (a) $t=0.5$ s; (b) $t=1.0$ s; (c) $t=1.5$ s; (d) $t=2.0$ s; (e) $t=2.5$ s; (f) $t=3.0$ s; (g) $t=3.5$ s; and (h) $t=4.0$ s.

5. NAVIER–STOKES SOLVER

Momentum and heat diffusion can be introduced to the flow solver by the inclusion of the necessary diffusive terms in the governing equations. These terms, from Equations (4) and (5), are functions of $\mathbf{u}$ and T, respectively, hence must be evaluated explicitly since the momentum and energy equations are solved for $\hat{\mathbf{u}}$ and $\hat{E}$, respectively. The resulting solution procedure would then be completely explicit: all new solutions at the current time level would be calculated from convection, diffusion and boundary conditions at the previous time level. This approach gives low computational cost per time step since it only requires a diagonal solver, but it can suffer a severe time step limit—increasingly so as diffusion dominates.

To remedy this we therefore apply sequential operator splitting to introduce the diffusive terms as implicit corrections to the original inviscid equations. For solution of both the momentum and energy equations, the following procedure is adopted: (1) solve the inviscid equation, where

DOI: 10.1002/fld

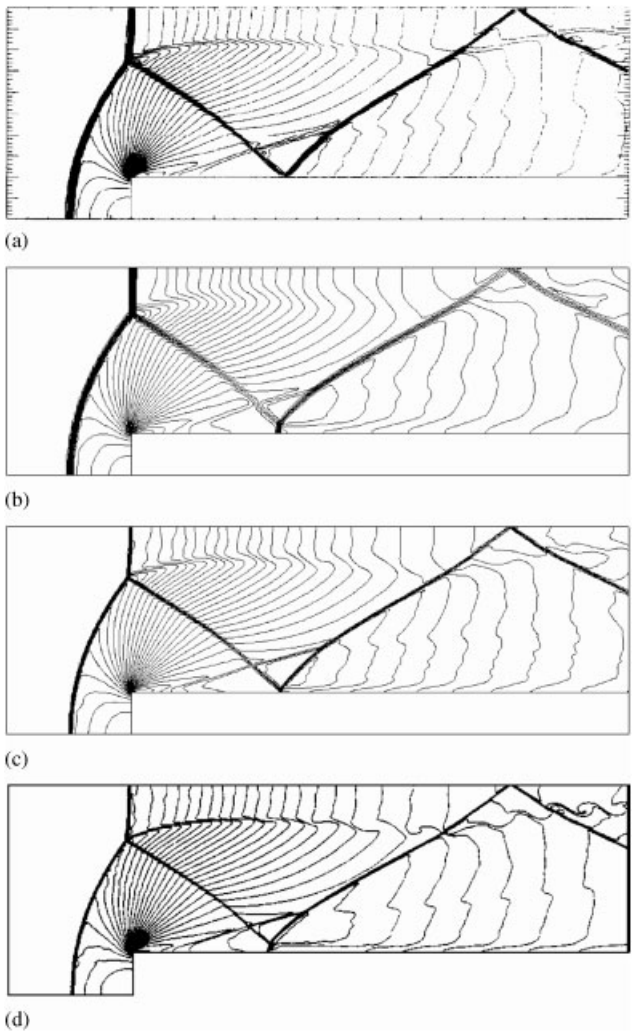

Figure 6. Forward-facing step; density solution at $t=4\,\mathrm{s}$; 30 contours in the range $0.2568<\rho<6.067$: (a) PPMLR, cell size $=\frac{1}{80}$ (after Woodward and Colella [32]); (b) KNP with van Leer, cell size $=\frac{1}{80}$; (c) KNP with van Leer, cell size $=\frac{1}{160}$; and (d) RKDG third order (P^2), cell size $=\frac{1}{160}$ (after Cockburn and Shu [8]).

the time derivative represents that due solely to inviscid fluxes, $(\partial/\partial t)_{\mathrm{I}}$; (2) update the primitive variable, e.g. $\mathbf{u}$ or T, that we wish to diffuse; (3) solve a diffusion correction equation implicitly for the primitive variable, where the time derivative represents that due to diffusion only, $(\partial/\partial t)_{\mathrm{V}}$. The solution of the momentum equation therefore proceeds by first solving for $\hat{\mathbf{u}}$:

$$\left(\frac{\partial \hat{\mathbf{u}}}{\partial t}\right)_{\mathrm{I}} + \nabla\cdot[\mathbf{u}\hat{\mathbf{u}}] + \nabla p = 0 \tag{18}$$

DOI: 10.1002/fld

(The momentum equation is represented above in its more 'physical' form, with the convective and pressure gradient terms separated, rather than combining their fluxes into a single divergence term. Please note, however, that the treatment of the fluxes in the numerical implementation of the equation ensures that it is strongly conservative.)

Velocity is then updated by $\mathbf{u}=\hat{\mathbf{u}}/\rho$ before solving a diffusion correction equation for $\mathbf{u}$

$$\left(\frac{\partial(\rho\mathbf{u})}{\partial t}\right)_{\mathrm{V}}-\boldsymbol{\nabla}\cdot(\mu\nabla\mathbf{u})-\boldsymbol{\nabla}\cdot(\mathbf{T}_{\mathrm{exp}})=0 \tag{19}$$

where terms in the stress tensor containing inter-component coupling are treated explicitly, $\mathbf{T}_{\mathrm{exp}}=\mu[(\nabla\mathbf{u})^{\mathrm{T}}-(\frac{2}{3})\,\mathrm{tr}(\nabla\mathbf{u})\mathbf{I}]$. The Laplacian term $\boldsymbol{\nabla}\cdot(\mu\nabla\mathbf{u})$ is implemented implicitly in $\mathbf{u}$, i.e. it forms coefficients within the solution matrix, rather than values in the source vector. Boundary conditions in $\mathbf{u}$ are also implemented implicitly, e.g. a gradient, or Neumann, condition is applied by direct substitution of the gradient at a boundary face.

The solution of the energy equation similarly proceeds by first solving for $\hat{E}$:

$$\left(\frac{\partial\hat{E}}{\partial t}\right)_{\mathrm{I}}+\boldsymbol{\nabla}\cdot[\mathbf{u}(\hat{E}+p)]+\boldsymbol{\nabla}\cdot(\mathbf{T}\cdot\mathbf{u})=0 \tag{20}$$

Temperature is then updated from $\hat{E}$, $\mathbf{u}$ and ρ according to Equation (16) before solving a diffusion correction equation for T:

$$\left(\frac{\partial(\rho c_v T)}{\partial t}\right)_{\mathrm{V}}-\boldsymbol{\nabla}\cdot(k\nabla T)=0 \tag{21}$$

Below we present the full algorithm for the Navier–Stokes solver in which μ and k are functions of T and updated within the iterative sequence.

Algorithm 1 Compressible flow solver

while $t<t_{\mathrm{end}}$ **do**
  Set $t:=t+\Delta t$
  Evaluate $\rho_{f\pm}$, $\hat{\mathbf{u}}_{f\pm}$ and $T_{f\pm}$ from ρ, $\hat{\mathbf{u}}$ and T using van Leer limiter
  Calculate: $\mathbf{u}_{f\pm}=\hat{\mathbf{u}}_{f\pm}/\rho_{f\pm}$; $p_{f\pm}=\rho_{f\pm}RT_{f\pm}$; $\phi_{f\pm}=\mathbf{S}_f\cdot\mathbf{u}_{f\pm}$; $c_{f\pm}=\sqrt{\gamma RT_{f\pm}}$.
  Calculate convective derivatives and ∇p from $f\pm$ interpolates using Eqs. (7) to (13)
  Update $\mathbf{T}_{\mathrm{exp}}$, μ and k
  Solve Equation (1) for ρ {density equation}
  Solve Equation (18) for $\hat{\mathbf{u}}$ {inviscid momentum prediction}
  Update $\mathbf{u}$ from $\hat{\mathbf{u}}$ and ρ
  Solve Equation (19) for $\mathbf{u}$ {diffusive velocity correction}
  Solve Equation (20) for $\hat{E}$ {inviscid energy prediction}
  Update T by Equation (16) from $\hat{E}$, $\mathbf{u}$ and ρ
  Solve Equation (21) for T {diffusive temperature correction}
  Update p by $p=\rho RT$
end while

DOI: 10.1002/fld

5.1. The supersonic jet problem (Ladenburg)

The supersonic jet problem we use as a test case is taken from Ladenburg *et al.* [35]. In their experiments, dry air was discharged into the open atmosphere from a pressurised tank through a circular nozzle that converges to 10 mm diameter at the exit orifice. The nozzle is essentially a tapered circular hole bored out of a cylindrical block of material [36] so that there is a flat solid wall in the plane of the exit orifice. Here, we examine the case in which the tank pressure is $60\,\mathrm{lb/in^2}$, or 4.14 bar, since it produces a Mach disc feature that is challenging to reproduce numerically. The inlet conditions at the nozzle throat were $p=2.72$ bar, $\mathbf{u}=(315.6,0,0)\,\mathrm{m/s}$ and $T=247.1\,\mathrm{K}$. Freestream conditions were $p=1.01$ bar, $\mathbf{u}=(0,0,0)\,\mathrm{m/s}$ and $T=297\,\mathrm{K}$. The thermodynamic properties for dry air used in the simulation were $R=287\,\mathrm{J/(kg\,K)}$ and $\gamma=1.4$. A Prandtl number $Pr=\mu c_p/k=0.75$ was assumed and the viscosity was modelled by Sutherland's Law:

$$\mu=A_s\frac{T^{1.5}}{T+T_s} \tag{22}$$

with $A_s=1.458\times10^{-6}\,\mathrm{Pa/K^{0.5}}$ and $T_s=110.4\,\mathrm{K}$.

The case is simulated as axisymmetric with a domain of height 10 mm, i.e. $2\times$ the orifice radius, and length 30 mm. A mesh of 240 cells along the length and 80 cells in the radial direction was used, which was sufficiently fine to produce a solution in which the location of the Mach disc did not change appreciably under further mesh refinement. The solver was run to a steady state at a CFL number of 0.5; typically, it took approximately 20 characteristic flow times to reach steady state, where the characteristic flow time is the time that a particle would take to travel the length of the geometry moving at the jet discharge velocity, i.e. approximately 2 ms in this case. The results in Figure 7 show contours of ρ with separation of $0.2\,\mathrm{kg/m^3}$. The air expands from the nozzle orifice from $\rho=3.8\,\mathrm{kg/m^3}$, creating a weak shock that extends from the orifice edge towards the nozzle axis. It approaches the axis at such a shallow angle (relative to the nozzle axis), that a

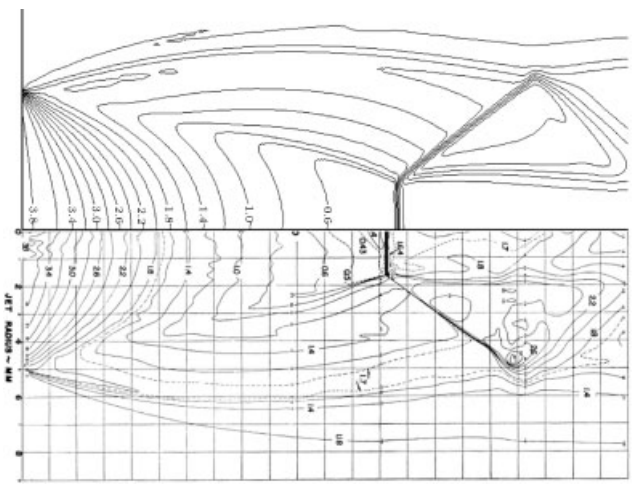

Figure 7. Density contours in the Ladenburg jet; our simulation (top) and original experimental data (bottom).

DOI: 10.1002/fld

Mach disc forms with a triple point at the intersection of the incident and reflected shocks, and the disc itself.

The data of Ladenburg, obtained by analysis of an interferogram, are reproduced in Figure 7, showing the triple point at (13.3, 1.7) mm. The results from our simulation show the triple point at (13.7, 1.64) mm, i.e. within $\sim 3\%$ of the experimental data. The error of 0.4 mm in the location in the x-direction seems to originate at the domain inlet, where the predicted contour at $\rho = 3.6$ is already displaced 0.4 mm in the downstream direction. It is possible that this error is caused by differences in the inlet conditions between the experiment and simulation.

5.2. Hypersonic flow over a 25°–55° *biconic (Holden and Wadhams)*

The case of hypersonic flow over a sharp 25°–55° biconic presents particular challenges that provide a good test for the accuracy of a numerical method. Here, we investigate Run 35 of the hypersonic flow experiments conducted in the Large Energy National Shock tunnel at the Calspan University at Buffalo Research Centre, specifically to provide data for code validation [37]. That experiment was conducted using nitrogen gas at low temperature and density. The freestream boundary conditions specified for this validation case are not directly measured but calculated from measured quantities in other regions of the tunnel using a quasi-one-dimensional computation. The conditions are $T = 138.9\,\mathrm{K}$, $p = 22.74\,\mathrm{Pa}$ and $\mathbf{u} = (2713, 0, 0)\,\mathrm{m/s}$, corresponding to a Mach number of 11.3. In our simulations, we used the Sutherland Law model for viscosity, Equation (22), with $Pr = 0.72$, $R = 296.8\,\mathrm{J/(kg\,K)}$ and $\gamma = 1.4$.

The case has been carefully simulated many times by other researchers [38–40] with results that consistently over predict the heat transfer along the leading cone surface. It is thought that this is mainly due to the free stream conditions being inaccurate, particularly because the original calculation did not account for a finite rate of relaxation of vibrational energy during expansion of the gas up to high Mach number [39]. While we adopt these specified free stream conditions in the knowledge that they are probably incorrect, it will allow us to compare results with those from other numerical schemes [40].

The physical aspects of the flow problem are best described by examining Figure 8, which show a cross section of the biconic with results from our simulations presented as blocks of a single colour, each representing a range of Mach number. An oblique shock forms from the 25° cone tip, located along the upper edge of the red region near its surface. A boundary layer develops along that surface which separates, creating a shock that interacts with the oblique shock and meets the bow shock from the 55° cone. A low-speed recirculation region forms at the junction between the 25° and 55° cones, clearly visible as the large blue triangle in the figure. Other features include a subsonic region downstream of the bow shock (blue) and a supersonic jet along the 55° cone surface (green).

The main challenge for the numerics in this case is the accurate prediction of the separation point along the 25° cone surface, and reattachment on the 55° cone surface, i.e. the overall length of the recirculation zone. Prediction of the length of the recirculation zone is extremely sensitive to the dissipation in the numerical scheme; the more the dissipation, the shorter the recirculation zone. It is therefore generally considered that better numerical schemes predict a larger recirculation zone, with solutions from the best schemes converging to 56.1 mm with mesh refinement [40].

We simulated this case as an axisymmetric geometry and boundary conditions. Our initial simulation used a mesh created by previous researchers [40] with ~ 32k cells, consisting of 256 grid points in the axial, streamwise direction and 128 points in the radial, wall normal direction. It

DOI: 10.1002/fld

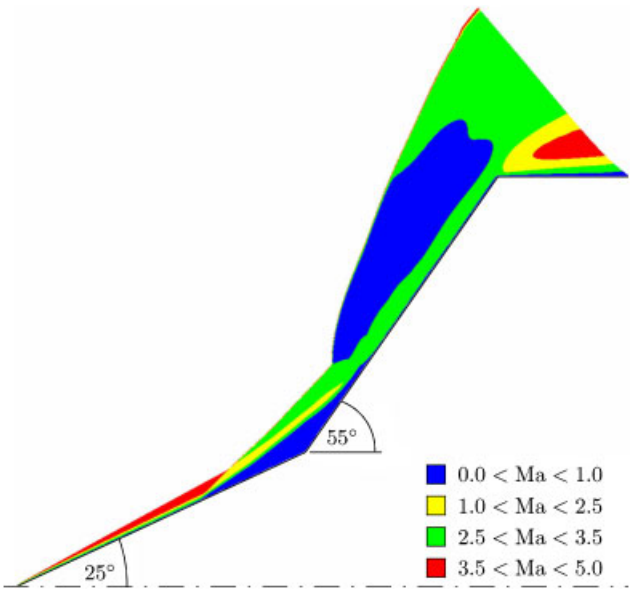

Figure 8. Mach number contour map for the 25°–55° biconic; 78 k cells; freestream Mach 11.3.

was carefully created with grading of cells towards the cone surface such that in the first column of cells, projecting radially from the 25° tip, the cell height ranges from $\sim 0.5\,\mu$m at the surface to ~ 0.2 mm at the upper boundary of the domain. This 256×128 mesh is considered coarse for the solution of this problem.

Careful time convergence studies show that the Run 35 case does not converge to steady state until after approximately 100 characteristic flow times are completed [41]; with the length of the double cone geometry being approximately 0.18 m, this equates to ~ 6.6 ms. We obtained steady-state results on the 256×128 mesh at 7 ms with a CFL number of 0.5.

Figure 9 shows the pressure distribution along the cone surface compared with the experimental data [37]. The surface pressure downstream of the oblique shock from the cone tip is predicted well. The separation point is predicted slightly further upstream than indicated by the increase in pressure at ~ 60 mm in the experiment. A pressure spike of ~ 7 kPa occurs at ~ 110 mm, consistent with the experimental measurements. Beyond that, the pressure oscillates at a frequency that is in good agreement with experiment, but with a larger amplitude.

Figure 10 compares our predicted surface heat flux with the experimental data. The heat flux along the leading edge of the 25° cone is overpredicted to a level consistent with results from other successful methods [40], which is believed to be primarily caused by using the incorrect freestream conditions, mentioned previously. The jumps in heat transfer across the recirculation region mirror those in pressure and the simulation show similar good agreement.

The comparisons with experimental data show that our method is competitive with the best methods previously published [38–40], namely modified Steger–Warming and a Roe solver with a number of limiters for gradient reconstruction, including van Leer and Minmod. By way of comparison, the recirculation zone size for the Roe solver with van Leer limiter was 49.1 mm, compared with 47.5 mm with our KNP solver with van Leer limiter. A Roe solver with Minmod

DOI: 10.1002/fld

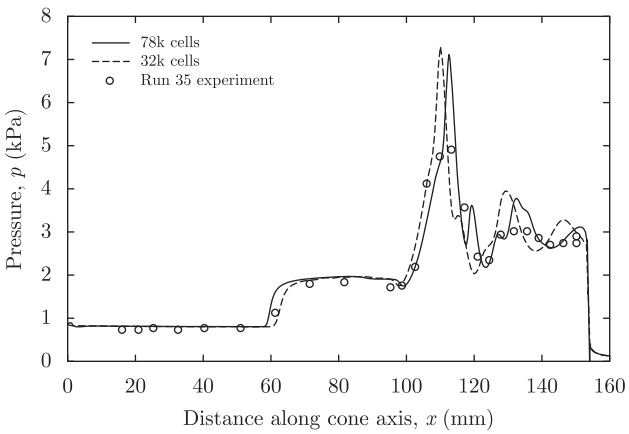

Figure 9. Surface pressure for the 25°–55° biconic, Run 35 configuration.

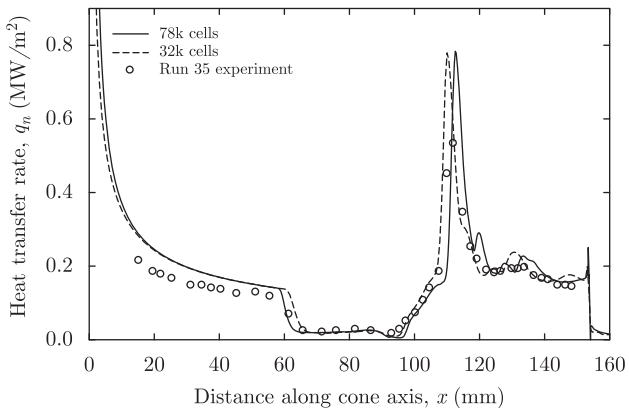

Figure 10. Surface heat transfer rate for the 25°–55° biconic, Run 35 configuration.

limiter gives a recirculation zone size of 42.2 mm. We can tentatively conclude that the accuracy of the KNP solver is close to that of an equivalent Roe solver.

In order to test the KNP method on polyhedral cells, the 256×128 mesh was refined by splitting cells in critical regions of the flow such as shocks, boundary layers and recirculation regions. The cells marked for splitting were initially those for which $|\nabla \rho| > 0.2\,\mathrm{kg/m^4}$. The regions of cells were then extended to include two additional layers of neighbouring cells covering a region shown in Figure 11(a). The cells were then split into 2×2 in the streamwise and wall normal directions, as shown in Figure 11(b).

Unsplit cells adjacent to a region of split cells have more than four faces lying in the circumferential plane. Faces connecting these polyhedral cells to hexahedra formed by the splitting process have appreciable non-orthogonality and skewness. Our refined mesh therefore contained ~ 78k cells, 40% fewer than the 130k cells that would have been obtained by a simple 2×2 refinement of all cells in the original mesh.

DOI: 10.1002/fld

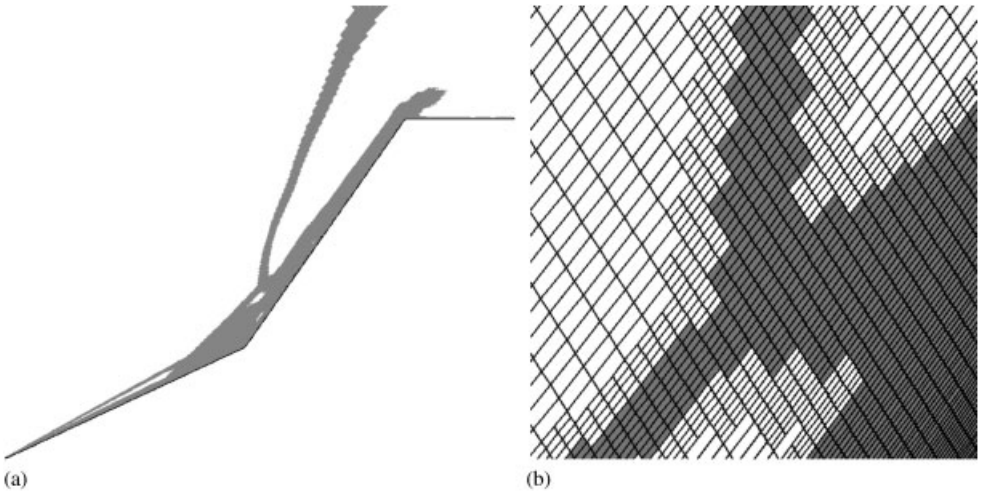

Figure 11. Adaptive mesh refinement for the 25°–55° biconic: (a) map of split cells and (b) split cells, grey: $|\nabla\rho|>0.2$.

Steady-state results for surface heat flux and pressure using this new 78 k cell mesh are also shown in Figures 9 and 10, respectively. (Additionally, the contour map of Mach number in Figure 8 was obtained using the 78 k cell mesh.) The results are broadly similar to those with the original 32 k cell mesh, with the exception that the recirculation zone has grown further to 52.6 mm. This is still a little shorter than 54.4 mm, the zone length predicted by a Roe solver with van Leer limiter [40] on a 130 k cell mesh. However, we can again conclude that the accuracy of the KNP solver is close to that of an equivalent Roe solver.

6. CONCLUSIONS

The details of an FV solver based on non-oscillatory central schemes have been presented. The KNP method offers clear improvements in accuracy over its predecessor, the KT method. We recommend as best practice to interpolate only ρ, $\hat{\mathbf{u}}$ and T in the $f+$ and $f-$ directions using the van Leer limiter, and derive other face-interpolated fields from these fields. Our new V-scheme offers a stable approach to limiting a vector field that is invariant under a coordinate transformation. Solution of momentum and energy transport is performed by a predictor equation for the convection of conserved variables followed by a corrector equation for diffusion of primitive variables. This enables the convection component to be solved quickly with a diagonal solver, while the diffusion component is solved implicitly to assist stability.

Results from four test simulations show the method presented is competitive with the best methods previously published. The 25°–55° biconic case is a particularly difficult CFD problem, but we were able to obtain good quality solutions. The mesh for that case was selectively refined by splitting cells in regions of high-density gradient, which increased the number of faces in layers of polygonal cells, and introduced some appreciable non-orthogonality. The performance of the KNP method with van Leer limiting did not appear to degrade on such meshes.

DOI: 10.1002/fld

ACKNOWLEDGEMENTS

CJG and JMR acknowledge the support of the UK's Engineering and Physical Sciences Research Council under grant EP/F014155/01. The authors wish to thank Steve Daley of Dstl Farnborough (UK). FLUENT is a registered trademark of ANSYS, Inc. STAR CCM+ is a registered trademark of Computational Dynamics Ltd. OPENFOAM is a registered trademark of OpenCFD Ltd.

REFERENCES

1. Ferziger JH, Peric M. *Computational Methods for Fluid Dynamics*. Springer: Berlin, Germany, 1996.
2. Versteeg HK, Malalasekera W. *An Introduction to Computational Fluid Dynamics*: *The Finite Volume Method*. Prentice-Hall: Englewood Cliffs, NJ, 1995.
3. Peric M, Ferguson S. The advantage of polyhedral meshes, 2005. Available from: http://www.cd-adapco.com/press_room/-dynamics/24/testVspoly.html.
4. van Leer B. Towards the ultimate conservative difference scheme, V: a second-order sequel to Godunov's method. *Journal of Computational Physics* 1979; **32**:101–136.
5. Colella P, Woodward P. The piecewise parabolic method (PPM) for gas-dynamical simulations. *Journal of Computational Physics* 1984; **54**:174–201.
6. Harten A, Engquist B, Osher S, Chakravarthy SR. Uniformly high order accuracy essentially non-oscillatory schemes III. *Journal of Computational Physics* 1987; **71**:231–303.
7. Liu XD, Osher S, Chan T. Weighted essentially non-oscillatory schemes. *Journal of Computational Physics* 1994; **115**:200–212.
8. Cockburn B, Shu CW. The Runge–Kutta discontinuous Galerkin method for conservation laws, V: multidimensional systems. *Journal of Computational Physics* 1998; **141**:199–224.
9. Nessyahu H, Tadmor E. Non-oscillatory central differencing for hyperbolic conservation laws. *Journal of Computational Physics* 1990; **87**:408–447.
10. Arminjon P, Viallon MC. Convergence of a finite volume extension of the Nessyahu–Tadmor scheme on unstructured grids for a two-dimensional linear hyperbolic equations. *SIAM Journal on Numerical Analysis* 1999; **36**:738–771.
11. Christov I, Popov B. New non-oscillatory central schemes on unstructured triangulations for hyperbolic systems of conservation laws. *Journal of Computational Physics* 2008; **227**:5736–5757.
12. Haasdonk B, Kroner B, Rohde D. Convergence of a staggered Lax–Friedrichs scheme for nonlinear conservation laws on unstructured two-dimensional grids. *Numerische Mathematik* 2001; **88**:459–484.
13. Huynh H. Analysis and improvement of upwind and centered schemes on quadrilateral and triangular meshes. *AIAA Paper 2003-3541*, *16th AIAA Computational Fluid Dynamics Conference*, Orlando, FL, 2003.
14. Katsaounis T, Levy D. A modified structured central scheme for 2D hyperbolic conservation laws. *Applied Mathematics Letters* 1999; **12**:89–96.
15. Kurganov A, Petrova G. Central-upwind schemes on triangular grids for hyperbolic systems of conservation laws. *Numerical Methods for Partial Differential Equations* 2005; **21**:536–552.
16. Kuther M. Error estimates for the staggered Lax–Friedrichs scheme on unstructured grids. *SIAM Journal on Numerical Analysis* 2001; **39**:1269–1301.
17. Arminjon P, Madrane A. St-Cyr A. Non-oscillatory Lax–Friedrichs type central finite volume methods for 3-D flows on unstructured tetrahedral grids. In *Hyperbolic Problems*: *Theory*, *Numerics*, *Applications*: *Eighth International Conference in Magdeburg*, February/March 2000, Freistühler H, Warnecke G (eds), vol. 140. Birkhäuser: Basel, 2001; 59–68.
18. Arminjon P, St-Cyr A. Nessyahu–Tadmor-type central finite volume methods without predictor for 3D Cartesian and unstructured tetrahedral grids. *Applied Numerical Mathematics* 2003; **46**:135–155.
19. Jiang GS, Tadmor E. Non-oscillatory central schemes for multidimensional hyperbolic conservation laws. *SIAM Journal on Scientific Computing* 1998; **19**:1892–1917.
20. Kurganov A, Lin CT. On the reduction of numerical dissipation in central-upwind schemes. *Communications in Computational Physics* 2007; **2**:141–163.
21. Kurganov A, Petrova G. A third-order semi-discrete genuinely multidimensional central scheme for hyperbolic conservation laws and related problems. *Numerische Mathematik* 2001; **88**:683–729.
22. Levy D, Puppo G, Russo G. Central WENO schemes for hyperbolic systems of conservation laws. *Mathematical Modelling and Numerical Analysis* 1999; **33**:547–571.

DOI: 10.1002/fld

23. Liu Y. Central schemes on overlapping cells. *Journal of Computational Physics* 2005; **209**:82–104.
24. Liu YJ, Shu CW, Tadmor E, Zhang M. Non-oscillatory hierarchical reconstruction for central and finite volume schemes. *Communications in Mathematical Physics* 2007; **2**:933–963.
25. Noelle S, Rosenbaum W, Rumpf M. 3D adaptive central schemes: part I. Algorithms for assembling the dual mesh. *Applied Numerical Mathematics* 2006; **56**:778–799.
26. Kurganov A, Tadmor E. New high-resolution central schemes for nonlinear conservation laws and convection–diffusion equations. *Journal of Computational Physics* 2001; **160**:241–282.
27. Kurganov A, Noelle S, Petrova G. Semi-discrete central-upwind schemes for hyperbolic conservation laws and Hamilton–Jacobi equations. *SIAM Journal on Scientific Computing* 2001; **23**:707–740.
28. Roe PL. Characteristic-based schemes for the Euler equations. *Annual Review of Fluid Mechanics* 1986; **18**: 337–365.
29. van Leer B. Towards the ultimate conservative difference scheme, II: monotonicity and conservation combined in a second order scheme. *Journal of Computational Physics* 1974; **17**:361–370.
30. OpenCFD Ltd, 2004. Available from: http://www.openfoam.org.
31. Sod G. A survey of several finite difference methods for systems of nonlinear hyperbolic conservation laws. *Journal of Computational Physics* 1978; **22**:1–31.
32. Woodward P, Colella P. The numerical simulation of two-dimensional fluid flow with strong shocks. *Journal of Computational Physics* 1984; **54**:115–173.
33. Anderson JD. *Modern Compressible Flow* (3rd edn). McGraw-Hill: New York, U.S.A., 2003.
34. Emery AE. An evaluation of several differencing methods for inviscid fluid flow problems. *Journal of Computational Physics* 1968; **2**:306–331.
35. Ladenburg R, van Voorhis CC, Winkler J. Interferometric studies of faster than sound phenomena. Part II. Analysis of supersonic air jets. *Physical Review* 1949; **76**:662–677.
36. Winkler J. The Mach interferometer applied to studying an axially symmetric supersonic air jet. *Review of Scientific Instruments* 1948; **19**:307–322.
37. Holden MS, Wadhams TP. Code validation study of laminar shock/boundary layer and shock/shock interactions in hypersonic flow. Part A: experimental measurements. *AIAA Paper 2001-1031A*, *39th Aerospace Sciences Meeting and Exhibit*, Reno, NV, 2001.
38. Harvey JK, Holden MS, Wadhams TP. Code validation study of laminar shock/boundary layer and shock/shock interactions in hypersonic flow. Part B: comparison with Navier–Stokes and DSMC solutions. *AIAA Paper 2001-1031B*, *39th Aerospace Sciences Meeting and Exhibit*, Reno, NV, 2001.
39. Candler GV, Nompelis I, Druguet MC, Holden MS, Wadhams TP, Boyd ID, Wang WL. CFD validations for hypersonic flight: hypersonic double-cone flow simulations. *AIAA Paper 2002-0581*, *40th Aerospace Sciences Meeting and Exhibit*, Reno, NV, 2002.
40. Druguet MC, Candler GV, Nompelis I. Effect of numerics on Navier–Stokes computations of hypersonic double-cone flows. *AIAA Journal* 2005; **43**:616–623.
41. Gaitonde DV, Canupp PW, Holden MS. Heat transfer predictions in a laminar hypersonic viscous/inviscid interaction. *Journal of Thermophysics and Heat Transfer* 2002; **16**:481–489.

DOI: 10.1002/fld